Available online at www.sciencedirect.com
SCIENCE DIRECT®
International Journal of Heat and Mass Transfer 47 (2004) 527–538
International Journal of HEAT and MASS TRANSFER
www.elsevier.com/locate/ijhmt

Modeling of pressure and shear-driven flows in open rectangular microchannels

S.W. Tchikanda *, R.H. Nilson, S.K. Griffiths

Fluid/Thermal Department, Sandia National Laboratories, Livermore, CA 94550, USA

Received 28 February 2003; received in revised form 3 July 2003

Abstract

Analytical expressions are derived for the mean velocity of a liquid flowing in an open rectangular microchannel. Solutions are decomposed into additive components driven by pressure gradients and by shear stresses on the liquid/vapor interface. Speeds are computed numerically for meniscus contact angles ranging from 0° to 90°, arbitrary channel aspect ratios, and for wetting regimes ranging from liquid-full to nearly-dry corner flows. These numerical results are used to guide the development of several analytical expressions that apply in asymptotic limits of fluid depth and contact angle. The resulting asymptotes are then blended analytically to obtain relatively simple, accurate, and comprehensive expressions for the mean velocity.
Published by Elsevier Ltd.

Keywords: Heat pipes; Microchannel flow; Fluid friction

1. Introduction

Liquid flow in microchannels is important to a number of technologies including cooling of microelectronics by heat pipes and capillary pumped loops as well as capillary wetting of channels in molding processes and in chip-based devices for identification of chemical and biological species. Since channel lengths in these applications greatly exceed lateral channel dimensions, such flows can be accurately and efficiently modeled using one-dimensional analyses in which the frictional flow resistance is described in terms of a friction coefficient that depends on the channel geometry, the fraction of the channel depth that is filled with liquid, and the wetting angle at the contact between the meniscus and the solid channel walls.

Although a number of previous numerical studies have provided friction coefficients for some subsets of the important parameter range, they generally do not span a wide range of channel aspect ratios and wetting angles and rarely do they provide accurate and comprehensive analytical approximations needed for application by others. Schneider and DeVos [1] analyzed the heat transport capability of axially grooved heat pipes. They presented an approximate model that includes the influence of liquid–vapor interaction and compared their results with the exact solution of DiCola [2]. However, these results are limited to cases in which the fluid depth is large compared to the radius of the meniscus. Suh et al. [3] investigated the flow of liquid and vapor in trapezoidal and sinusoidal grooves, taking into account the effects of variable shear stress at the interface. They modified the approximate relation for the friction in rectangular grooves which was developed by Schneider and DeVos [1] to obtain approximations for the trapezoidal and sinusoidal grooves that are accurate within limited parameter ranges ($0.65 \leqslant W/h \leqslant 2$, $0° \leqslant \alpha \leqslant 60°$). Thomas et al. [4] presented a semi-analytical solution and a two-point numerical solution for the mean velocity in trapezoidal grooves with shear stress at the liquid–vapor interface. Although comprehensive, the suggested analytical approximations may yield errors as large as 30%.

In addition to these studies of flows in rectangular microchannels, there have been several studies describing

* Corresponding author. Tel./fax: +1-925-294-4784.
E-mail address: swtchik@sandia.gov (S.W. Tchikanda).

0017-9310/$ - see front matter Published by Elsevier Ltd.
doi:10.1016/j.ijheatmasstransfer.2003.03.001

Nomenclature

A	cross-sectional area
c	coefficient defined by Eq. (30)
D	microchannel height
E	aspect ratio, D/W
g	gravitational acceleration
h	meniscus height at the symmetry line
H	meniscus height at the wall
L	dimension defined by Eq. (5)
$\hat{n}$	free surface unit outward normal
p	pressure
R	free surface radius
S	liquid area fraction
u	axial velocity component
U	mean velocity
W	microchannel width
x,y,z	Cartesian coordinates

Greek symbols

α	contact angle
γ	surface tension coefficient
θ	angle defined by Eq. (4)
λ	aspect ratio, W/h
Λ	aspect ratio defined by Eq. (3)
μ	liquid viscosity
ρ	liquid density
τ	shear stress at liquid–vapor interface

Subscripts

C	corner flow
p	pressure solution
τ	shear solution
x	averaged over y
0	value at $\alpha = 0°$
1	left asymptote
2	right asymptote

Superscript

*	dimensionless variable

flow and heat transfer in triangular grooves. Many of these are focused on the performance of evaporative cooling devices [5–7]. Furthermore, the papers by Ayyaswamy et al. [8], Ransohoff and Radke [9], and Romero and Yost [10] explore frictional relationships for triangular grooves. The last of these provides useful analytical approximations for flows in triangular domains that complement the present results. In particular, those previous results for an apex angle of 90° describe flows in the corners of rectangular channels and as such represent end-member solutions in the spectrum of configurations that we address here.

In the present paper we use numerical solutions of the Navier–Stokes equations to guide the construction of analytical approximations that are based upon blending of asymptotic solutions that apply in the limits of small and large ratios of channel width to fluid depth and in the limits of small and large contact angles. The overall solutions are decomposed into two components. The first of these is the flow driven by pressure gradients that may result from capillary forces, gravity, or applied pressures. The second component is the flow driven by shear stresses on the liquid–vapor interface. This second component is sometimes important for parallel flows of liquid and vapor in heat pipes and capillary pumped loops. The resulting composite expressions obtained by blending asymptotic solutions are quite comprehensive in their range of application. They are relatively easy to apply and are accurate within a few percent over the parameter ranges relevant to most practical applications.

2. Flow configurations

The steady flow of an incompressible Newtonian liquid is considered for the rectangular groove geometry shown in Fig. 1. These straight-sided channels are particularly important in heat transfer applications because high-aspect-ratio channels having parallel walls can be fabricated readily from high-conductivity metals using lithographic and electrodeposition processes [11].

The free surface between the liquid and the vapor has a constant radius of curvature when the channel width, W, is considerably less than the characteristic capillary length, $(\gamma/\rho g)^{1/2}$, where γ is the surface tension, ρ is the

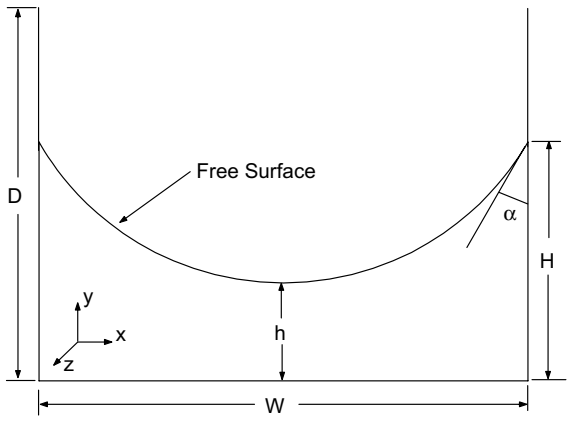

Fig. 1. Rectangular groove geometry and coordinate system.

density, and g is the gravitational acceleration. This condition is typically met for sub-millimeter channel widths. Under this restriction and for contact angles less than 90°, the free surface shape is circular and in accordance with the geometry of Fig. 1 is given by

$$y = H + \frac{W}{2}\tan\alpha - \sqrt{\frac{W^2}{4\cos^2\alpha} - x^2}, \tag{1}$$

where x and y are measured from the center of the channel bottom, the radius of the circle is $W/(2\cos\alpha)$, and the circle is centered at $x = 0$ and $y = H + (W/2)\tan\alpha$.

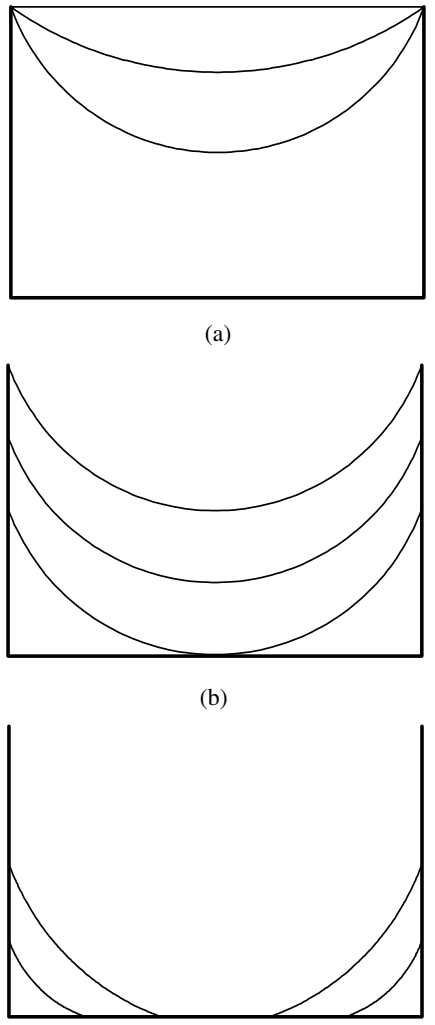

Fig. 2. Sequence of flow configurations in a microchannel. (a) Liquid recedes into channel with increasing contact angle of meniscus pinned at top edges. (b) Liquid recedes toward bottom of channel with constant contact angle and surface curvature. (c) Liquid recedes into the corners with constant contact angle.

Three different flow configurations are identified in the cross-sectional xy-planes shown in Fig. 2. All three of these may apply over different axial sections of the same channel, as in transient wetting processes or evaporating flows where the fluid depth decreases along the channel. In the configuration of Fig. 2a, the meniscus remains attached to the top edge of the channel and the contact angle may vary freely so long as it remains greater than the minimum contact angle that is dependent upon the liquid and solid surface energies. For lesser amounts of fluid within the channel the interface recedes toward the bottom of the groove with a constant contact angle, and thus a constant radius of curvature, as shown in Fig. 2b. If the meniscus reaches the bottom of the groove, the flow splits into a pair of corner flows that may further recede into the corners of the groove as shown in Fig. 2c.

The transition from a single meniscus that spans the channel into separate corner menisci must conserve mass and must also preserve the contact angle between the free surface and the groove side wall. This transition is continuous only for a minimum contact angle of 0° since this is the only case where the meniscus has a contact angle of 0° at the bottom center of the channel just before and just after the meniscus touches the bottom. For contact angles $\alpha \neq 0°$ the free surface exhibits a jump when the liquid splits into separate corner flows. Note that for contact angles $\alpha > 45°$ the free surface curvature changes from concave up to concave down upon transition into a corner.

The primary dependent variables in one-dimensional modeling of microchannel flows are typically the pressure, mean fluid speed, and the liquid area fraction or saturation, representing the fraction of the channel cross-section that is filled with liquid. The liquid speed is related to the pressure gradient through a local friction factor or a dimensionless speed that must be known as a function of the local saturation which, in turn, must be related to the fluid depth within the channel. For the rectangular groove shown in Fig. 1, the saturation is given by

$$S = \frac{2L^2}{WD}\left[\frac{H}{L} - \frac{1}{\Lambda} - \frac{\pi - 2(\alpha+\theta) - \sin[2(\alpha+\theta)]}{8\cos^2\theta\cos^2(\alpha+\theta)}\right], \tag{2}$$

where

$$\Lambda = \frac{2L}{H-h} = \frac{2\cos\alpha}{1-\sin\alpha}, \tag{3}$$

$$\tan\theta = \frac{H-h}{L} = \frac{2}{\Lambda}, \tag{4}$$

and

$$L = \begin{cases} W/2 & \text{when meniscus spans channel,} \\ H & \text{for the separate corner flow.} \end{cases} \tag{5}$$

It is instructive to note that for corner flows, $\tan\theta = 1$ regardless of the value of α and thus $\Lambda = 2$ so that

$$S = \frac{H^2}{WD}\left[1 - \frac{\pi - 2(\alpha+\theta) - \sin[2(\alpha+\theta)]}{4\cos^2\theta\cos^2(\alpha+\theta)}\right]. \quad (6)$$

3. Governing equations

For fully developed laminar flow at low Reynolds numbers, the governing Navier–Stokes equations reduce to a balance between the axial pressure gradient and the viscous shear stresses in the cross-sectional plane. Thus,

$$\frac{\partial^2 u}{\partial x^2} + \frac{\partial^2 u}{\partial y^2} = \frac{1}{\mu}\frac{\partial p}{\partial z}, \quad (7)$$

where u is the velocity component in the axial direction, μ is the viscosity of the fluid, and p is the pressure. Shear forces due to axial velocity variations are neglected because channel lengths generally exceed lateral dimensions by orders of magnitude.

On the groove walls, the no-slip condition is imposed,

$$u = 0, \quad (8)$$

while the boundary condition on the liquid–vapor interface is

$$\mu\nabla u \cdot \hat{\boldsymbol{n}} = \tau, \quad (9)$$

where $\hat{\boldsymbol{n}}$ is the unit outward normal to the interface and τ is the shear stress.

The momentum equation is made dimensionless by introducing the following dimensionless variables:

$$x^* = \frac{x}{W}, \quad y^* = \frac{y}{h}, \quad u^* = \frac{-u\mu}{W^2(\partial p/\partial z)}, \quad \tau^* = \frac{-\tau}{W(\partial p/\partial z)}. \quad (10)$$

Under this scaling, the momentum balance and free surface boundary condition, Eqs. (7) and (9), take the form

$$\frac{\partial^2 u^*}{\partial x^{*2}} + \lambda^2\frac{\partial^2 u^*}{\partial y^{*2}} = -1 \quad (11)$$

and

$$\nabla u^* \cdot \hat{\boldsymbol{n}}^* = \tau^*, \quad (12)$$

where the aspect ratio is

$$\lambda \equiv \frac{W}{h}. \quad (13)$$

Because Eqs. (11) and (12) are linear, the solution can be decomposed into a pressure-driven flow solution, u_p^*, that satisfies

$$\frac{\partial^2 u_p^*}{\partial x^{*2}} + \lambda^2\frac{\partial^2 u_p^*}{\partial y^{*2}} = -1, \quad (14)$$

with zero shear on the liquid–vapor interface,

$$\nabla u_p^* \cdot \hat{\boldsymbol{n}}^* = 0, \quad (15)$$

and a shear-driven flow solution, u_τ^*, that satisfies

$$\frac{\partial^2 u_\tau^*}{\partial x^{*2}} + \lambda^2\frac{\partial^2 u_\tau^*}{\partial y^{*2}} = 0, \quad (16)$$

subject to a dimensionless boundary condition that assumes a uniform shear stress along the interface,

$$\hat{\boldsymbol{n}}^* \cdot \nabla u_\tau^* = 1. \quad (17)$$

Thus, the combined solution can be expressed as

$$u^* = u_p^* + u_\tau^*\tau^*. \quad (18)$$

Eqs. (14)–(17) show that the solutions u_p^* and u_τ^* are independent of the magnitude of the interfacial shear stress and depend only on the geometry of the channel and the free surface.

Since gas viscosities are generally orders of magnitude smaller than liquid viscosities, interfacial shear forces will often be very small compared to those on the channel walls, particularly when the channel is relatively deep. It is for this reason and for simplicity that we have assumed uniformity of the shear stress over the interface with the understanding that this represents the average of an interfacial stress that may vary across the interface. Since our ultimate goal is the formulation of one-dimensional models, an estimate of the interfacial stress on the liquid can be based on the relative speed of the one-dimensional gas flow above the liquid.

The governing equations were solved numerically to obtain axial velocity distributions like those shown in Figs. 3 and 4 for different aspect ratios and contact angles. This was accomplished by discretizing the governing equations on a nonuniform grid using the finite volume method. To verify our numerical results calculations were performed to obtain the friction factor coefficient for the triangular groove problem studied by Ayyaswamy et al. [8] as well as the rectangular groove problem studied by Schneider and DeVos [1]. By successive grid refinements we obtained agreement within 0.1% over the full range of parameters they considered. For the results reported in this paper, the gridding was chosen so that a doubling of the grid points altered the computed mean speed by less than 0.5%, an error smaller than the deviations between our numerical results and analytical approximations given in the next sections.

The dimensionless mean velocities are obtained by averaging the axial velocity profiles over the channel cross-section

$$U^* = \frac{1}{A}\int\int_A u^*(x^*, y^*)\,\mathrm{d}A. \quad (19)$$

Note that this average is taken over the portion of the channel that is occupied by the liquid so that the mass

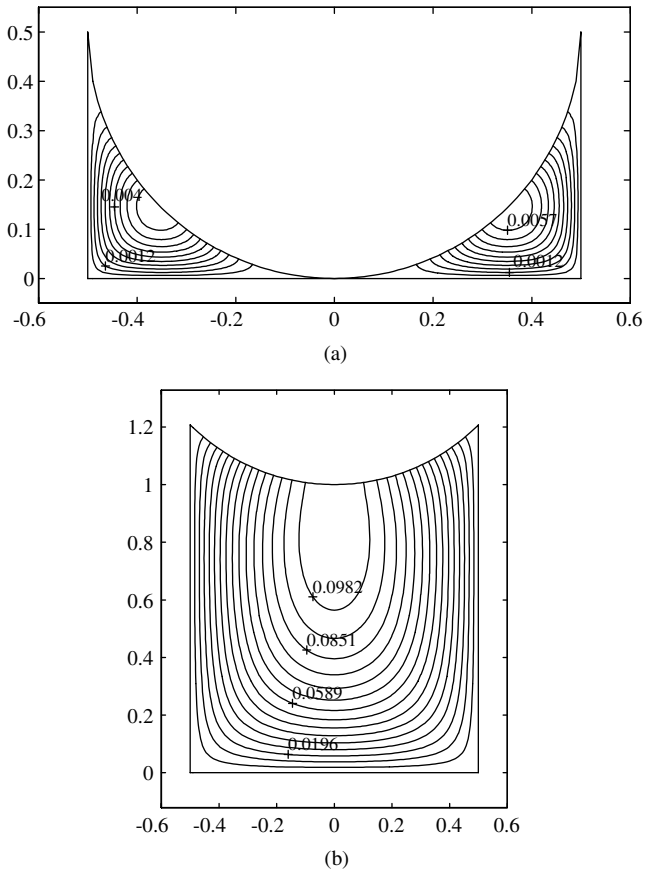

Fig. 3. Axial velocity contours for pressure-driven flow: (a) $\alpha = 0°$, $h = 0$; (b) $\alpha = 45°$, $h = 1$.

flux of the liquid may be written as ρASU, where A is the full cross-sectional area and S is the liquid area fraction. The friction factor, f, is related to the dimensionless mean velocity by

$$f \cdot Re = \frac{D_h^{*2}}{2U^*}, \tag{20}$$

where $Re = \rho u D_h/\mu$ is the Reynolds number, D_h is the hydraulic diameter and $D_h^* = D_h/W$.

4. Results for pressure-driven flow

Fig. 5a shows the mean velocity as a function of aspect ratio for several choices of the contact angle. As λ approaches zero, all the curves collapse onto a single well-known asymptote, $U^* = 1/12$. In this limit the depth of the fluid greatly exceeds the channel width and the flow resembles that between parallel planes of infinite extent. Since the depth of the meniscus region is small compared to the overall fluid depth, there is no dependence on the contact angle in this regime. The downward sloping intermediate asymptote shown in Fig. 5a is given by $U^* = 1/3\lambda^2$. As explained in Appendix A, this solution is applicable for fluid layers having a depth much smaller than the channel width such that the pressure gradient is balanced by the shear stress on the channel floor. With increasing λ, the curves in Fig. 5a transition from the left hand asymptote onto the intermediate asymptote, $U^* = 1/3\lambda^2$, until finally turning onto separate horizontal asymptotes, $U_C^*(\alpha)$, describing corner flows like that shown in Fig. 3a.

The corner flows depicted in Figs. 2c and 3a become applicable in the limit as $h \to 0$ and hence $\lambda \to \infty$ and so these appear as the horizontal asymptotes on the right side of Fig. 5a. For convenience, these corner flow solutions may be characterized by the alternate aspect ratio $\Lambda = W/H$, where H is the height of the meniscus at its contact with the side wall. The relationship between Λ and α is given by Eq. (3). The advantage of parameterization in terms of Λ rather than α is that the mean velocities of the corner flows may be viewed as a transition between asymptotes that apply in the limits as $\Lambda - 2 \to 0$ (i.e. $\alpha \to 0$) and $\Lambda \to \infty$ (i.e. $\alpha \to 90°$), as

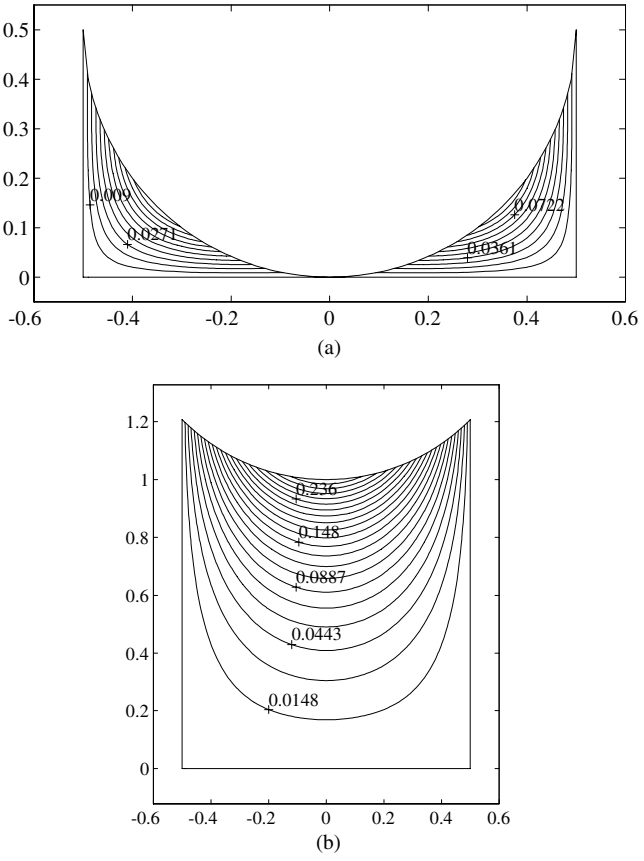

Fig. 4. Axial velocity contours for shear-driven flow: (a) $\alpha = 0°$, $h = 0$; (b) $\alpha = 45°$, $h = 1$.

seen in Fig. 5b. The left hand asymptote is given by $U_C^* = 0.0027$. This is the mean speed for a corner flow having a contact angle of 0°; velocity contours for this case were shown earlier in Fig. 3a. This numerical result was also checked against that obtained by Ransohoff and Radke [9]. The right hand asymptote in Fig. 5b is given by $U_C^* = 1/7\Lambda^2$ as $\Lambda \to \infty$. This result, derived in Appendix A, is based on two observations that apply in this limit: first, that the meniscus profile is well approximated by a parabola and, second, that the liquid layer becomes shallow such that the flow is resisted mainly by the shear stress on the bottom surface.

All of the asymptotic solutions explained above and in Appendix A are blended analytically to obtain a relatively simple and accurate expression for the mean velocity as a function of contact angle and aspect ratio. The blend is obtained using the following expression that applies to any pair of asymptotes, U_1^* and U_2^*:

$$U^* = \left[\frac{(U_1^* U_2^*)^m}{(U_1^*)^m + (U_2^*)^m}\right]^{1/m}. \tag{21}$$

The expression in Eq. (21) reduces to U_1^* in the limit when $U_1^* \ll U_2^*$ and, conversely, reduces to U_2^* when $U_2^* \ll U_1^*$. The parameter m controls the shape of the transition between the asymptotes.

For the corner flow solutions shown in Fig. 5b, the left and right asymptotes U_1^* and U_2^* are defined by

$$U_1^* = U_{C,0}^* = 0.0027, \tag{22}$$

$$U_2^* = \frac{1}{7(\Lambda-2)^2 + b(\Lambda-2)^k}. \tag{23}$$

The first of these is simply the corner flow that applies when $\alpha = 0°$ (i.e. $\Lambda = 2$ as seen from Eq. (3)). Since $\Lambda = 2$ is the minimum possible value of Λ for a spanning meniscus, the independent variable used in the asymptotic blending should be taken as $\Lambda - 2$. The right hand solution, U_2^*, reduces to the correct asymptote, $1/7\Lambda^2$, in the limit as $\Lambda \to \infty$. The additional term included in the denominator could be omitted but provides the flexibility to improve the fit without affecting the asymptotic behavior in either limit, provided $k < 2$. The blended result

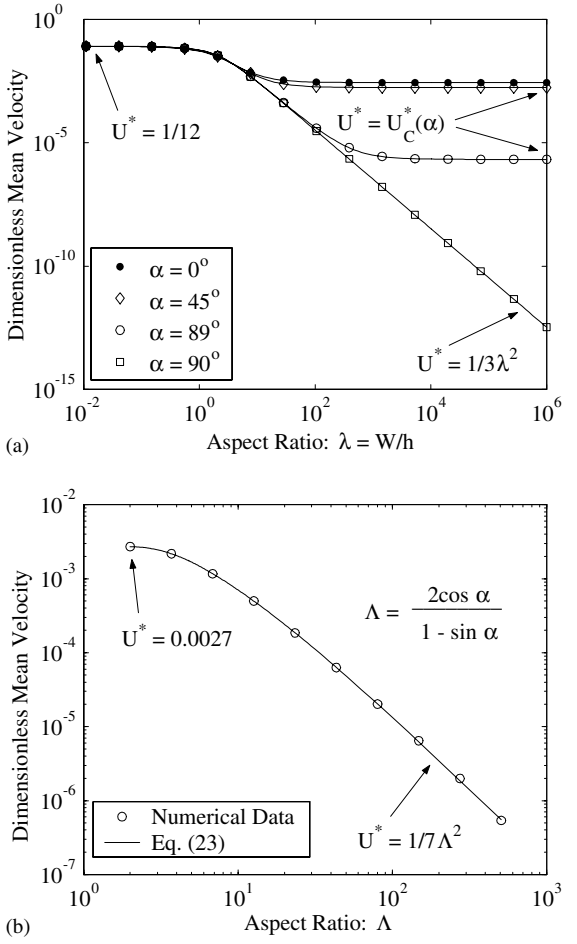

Fig. 5. Dimensionless mean velocity as a function of aspect ratio for the pressure-driven flow: (a) aspect ratio based on fluid depth at channel center; (b) corner flow solutions for zero depth at channel center.

$$U_C^* = \left\{ \frac{(U_{C,0}^*)^m}{1 + (U_{C,0}^*)^m [7(\Lambda - 2)^2 + b(\Lambda - 2)^k]^m} \right\}^{1/m}, \quad (24)$$

is accurate to within 2% relative error with the parameters m, b, and k set to 1.88, 150, and 0.87, respectively. The relative error is defined by the difference between the numerical result and the analytical approximation divided by the numerical result. Thus, the accuracy of the blending approximations is defined with respect to the numerical solutions of the governing equations given in Section 3.

To obtain a comprehensive expression describing the mean velocity for all contact angles and aspect ratios, the asymptotes U_1^* and U_2^* are chosen as

$$U_1^* = \frac{1}{12}, \quad (25)$$

$$U_2^* = \left[\left(\frac{1}{a\lambda + 3\lambda^2} \right)^n + (U_C^*)^n \right]^{1/n}. \quad (26)$$

The left asymptote, U_1^*, applies to very deep channels while the right asymptote, U_2^*, ultimately approaches one of two alternative limits as the liquid layer becomes shallow and $\lambda \to \infty$. The corner flow solution is recovered for any finite U_C; otherwise, the mean speed decreases as $1/3\lambda^2$, as appropriate for a contact angle of 90°. As explained earlier, the linear term is added to improve the fit without disturbing the asymptotes. When Eqs. (25) and (26) are substituted into Eq. (21) with the parameters $m = 1.31$, $n = 0.82$, and $a = 8.37$, the mean velocity can be approximated with a maximum relative error of 10% for α in the range $0° \leqslant \alpha \leqslant 60°$. Different sets of (m, n, a) can be used to obtain different levels of accuracy over various ranges of the contact angle. For the familiar case of a relatively wide channel (i.e. $W \gg (\gamma/\rho g)^{1/2}$) having a flat interface over most of the channel width, or equivalently for narrow channels with $\alpha \approx 90°$, the parameters $m = 1$, $n = 1$, and $a = 2.6$ yield a relative error of 2.5%. In heat pipes and other capillary pumping applications where small contact angles are of great importance, the parameters $m = 1.4$, $n = 0.83$, and $a = 9.71$ yield a maximum relative error of only 6% for contact angles in the range $0° \leqslant \alpha \leqslant 30°$.

Since one-dimensional flow models often utilize the saturation or liquid area fraction as a dependent variable, it is useful to plot the mean speed as a function of the saturation. This is done in Fig. 6 for different values of the contact angle and the aspect ratio, $E = D/W$, where D is the full depth of the channel rather than the

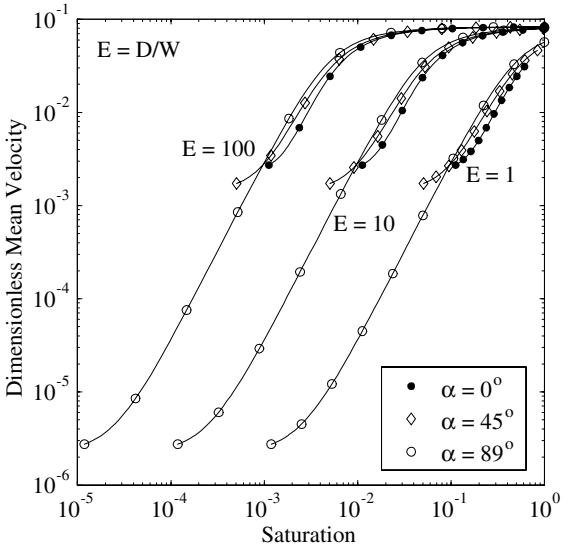

Fig. 6. Dimensionless mean velocities vs. saturation for pressure-driven flow.

liquid depth. As the saturation approaches unity, all of the results tend toward the asymptotic value of 1/12, descriptive of flow between parallel walls, although the result for $E = 1$ always remains well below this limit because frictional forces on the channel floor always remain important in shallow channels. Note that the maximum saturation cannot reach unity for contact angles less than 90° because the concave meniscus prevents complete filling.

With decreasing saturation, and hence decreasing fluid depth, the mean speed decreases as the friction on the channel floor progressively influences a greater fraction of the fluid within the channel. As the depth becomes sufficiently shallow, the mean fluid speed becomes proportional to the square of the depth whereas the saturation is simply proportional to the depth. Hence the mean speed grows as the square of the saturation, as apparent in the straight sections having a slope of 2 in Fig. 6. This regime, corresponding to the $1/3\lambda^2$ asymptote noted earlier in Fig. 5a, is mainly a feature of flows having a contact angle approaching 90°. For contact angles less than 90°, the saturation decreases to a finite value corresponding to the corner flows discussed earlier. For geometric reasons, the saturations corresponding to these corner flows are larger for smaller values of both the aspect ratio, E, and the contact angle.

As explained earlier, for saturations smaller than those shown in Fig. 6, the separate flows in the opposing corners must have equal contact angles on the bottom and side walls and their mean speeds are given by the solutions presented in [8–10]. Since the mean speed and the flow area of these equilateral corner flows are both proportional to the square of the wetted length along the walls, the speed is simply proportional to the saturation in this regime.

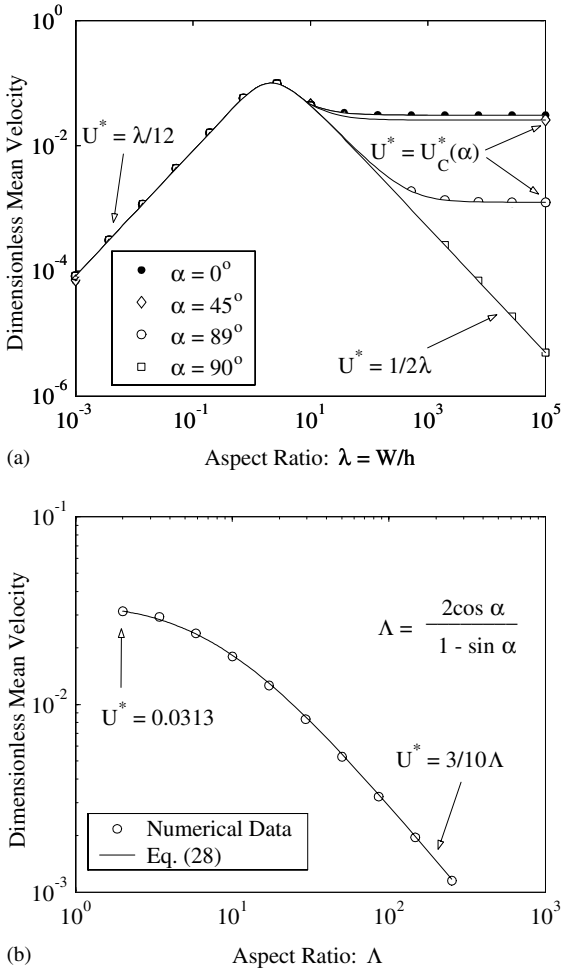

Fig. 7. Dimensionless mean velocity as a function of aspect ratio for the shear-driven flow: (a) solutions at different contact angles; (b) corner flow solutions.

5. Results for shear-driven flow

Fig. 7a shows the mean velocity of shear-driven flows as a function of aspect ratio for several choices of the contact angle. As in the preceding pressure-driven flows, several asymptotic regimes are readily identified and these can be blended to construct composite expressions for the mean velocity.

The corner flow solutions for this case are shown in Fig. 7b. As before, the left hand asymptote of the corner flows is simply a constant, and the right hand asymptote is derived by considering the flow in a thin layer having a parabolic meniscus, as appropriate for contact angles approaching 90°. As explained in Appendix A, the shear stress in this thin layer is uniform through the depth and equal to the applied unit stress at the free surface. Thus, the maximum speed at the surface and the mean speed are both directly proportional to the layer depth. Integration across the channel yields a mean speed of $U_2^* = 3/10\Lambda$. These two asymptotic results are first written in terms of the independent variable $\Lambda - 2$,

$$U_1^* = U_{C,0}^* = 0.0313, \tag{27}$$

$$U_2^* = \frac{3}{10(\Lambda - 2)}, \tag{28}$$

and then substituted into Eq. (21) to yield

$$U_C^* = \left\{ \frac{(U_{C,0}^*)^m}{1 + \left[\frac{10}{3}(\Lambda - 2)U_{C,0}^*\right]^m} \right\}^{1/m}. \tag{29}$$

When the parameter $m = 1.11$, Eq. (29) approximates the mean velocities of the shear-driven corner flow to within 4% relative error.

Unlike pressure-driven flows, shear-driven flows in deep channels have mean speeds that decrease linearly with the fluid depth, as seen on the left hand side of Fig. 7a. This behavior is predicted by a Fourier series solution, given in Appendix A, that yields a mean speed of exactly $\lambda/12$ for a contact angle of 90°. The observed reduction of mean speed with liquid depth occurs because the driving shear force is applied only at the top surface whereas the resistive shear forces on the side walls act at all depths. As a result, local speeds decrease exponentially with distance below the surface, as apparent in the contour plots of Fig. 4b. For sufficiently deep channels, the flow is essentially stagnant at depths more than two or three channel widths below the top surface and, regardless of the overall depth, the flow near the top remains the same. Thus, further increases in channel depth cause a reduction in the mean speed because the total fluid flow rate in the numerator of Eq. (19) remains unchanged, while the total fluid-filled area in the denominator continues to increase linearly with the overall fluid depth.

Because the shear-driven flows are dominated by the near surface layer, the mean speed is somewhat sensitive to the contact angle, even when the layer is deep. This is apparent in the moderate separation between the left hand asymptotes in Fig. 7a. This set of parallel asymptotes is very accurately approximated by $U_1^* = \lambda/c$ where the constant is given by the following function of the contact angle,

$$c(\alpha) = -1.55\alpha^2 + 0.84\alpha + 14.57, \quad 0 \leqslant \alpha \leqslant \pi/2. \tag{30}$$

A composite expression for the mean speed of shear-driven flows is constructed by blending the left hand asymptotes of the preceding paragraph with the corner flow solutions discussed earlier in the context of Fig. 7b. In addition, it is necessary that the mean speed decrease as $1/2\lambda$ as $\lambda \to \infty$ for a contact angle approaching 90°; this shallow-layer limit is derived in Appendix A. Thus, to accommodate all three of these asymptotes, we select the following expressions analogous to those given by Eqs. (25) and (26) for pressure-driven flow.

$$U_1^* = \frac{\lambda}{c}, \tag{31}$$

$$U_2^* = \left[\left(\frac{1}{2\lambda + \mathrm{d}\lambda^k}\right)^n + (U_C^*)^n\right]^{1/n}. \tag{32}$$

When Eqs. (31) and (32) are substituted into Eq. (21) with the parameters $m = 1$, $n = 1.75$, $d = 1$, and $k = 0.6$ the mean velocity can be approximated with a maximum relative error of 15% for α in the range $0° \leqslant \alpha \leqslant 90°$. For contact angles in the range $85° \leqslant \alpha \leqslant 90°$ the parameters $m = 2.6$, $n = 1.4$, $d = 5.9$, and $k = -0.3$ yield a relative error of 5%. For contact angles in the range $0° \leqslant \alpha \leqslant 30°$ the parameters $m = 1.1$, $n = 1.38$, $d = 2$, and $k = 0.9$ yield a maximum relative error of only 5%.

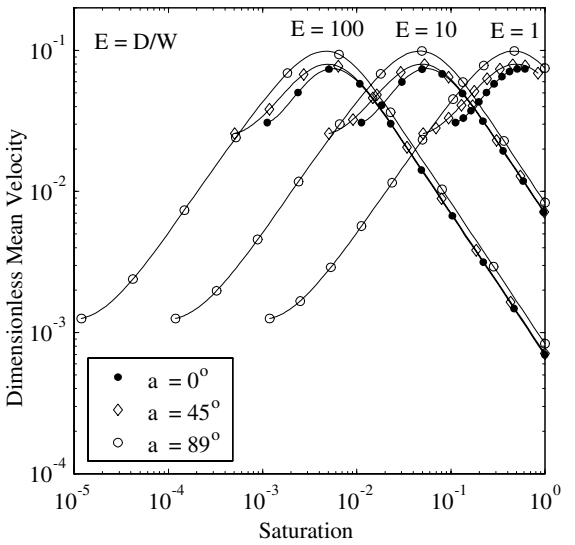

Fig. 8. Dimensionless mean velocities vs. saturation for shear-driven flow.

Fig. 8 shows the mean velocity of shear-driven flows as a function of saturation for various contact angles and aspect ratios, $E = D/W$. In analogy with Fig. 7a, mean speeds are generally highest for intermediate values of the fluid depth, or equivalently, the saturation. At small saturations, the shallow liquid layer is impeded by shear on the channel floor. Conversely, at large saturations only the top portion of the liquid layer is in motion such that the mean speed decreases with increasing saturation whenever the layer depth is greater than about one channel width. As a result, the mean speed decreases linearly with saturation for all saturations greater than about 0.1 and 0.01, respectively, in channels having aspect ratios, E, of 10 and 100.

An important conclusion to be drawn from Figs. 7a and 8 is that surface shear forces are generally much less important than pressure forces whenever fluid layer depths exceed one or two channel widths. This is because the surface shear has little influence beyond a depth of two or three channel widths, whereas pressure forces act with equal strength at all depths. In capillary-driven evaporative cooling device, deep fluid layers are generally beneficial since they provide greater mass flow and, hence, greater cooling ability. In addition, these deep layers are less susceptible to retardation by the shear forces of a countercurrent vapor flow, as occurs in many heat pipe devices. Indeed, for channel aspect ratios greater than about $E = 10$, surface shear affects will have little influence on the mean fluid speed until the channel is nearly dry. It should be noted, however, that increases in channel depth cause an increase in the temperature difference required to conduct heat from the channel

base to the meniscus. Thus, the device design must incorporate an optimal balance between these opposing considerations.

6. Conclusions

The mean velocity of a liquid flowing in a rectangular microchannel has been investigated both numerically and analytically for contact angles ranging from 0° to 90° and for the full spectrum of channel aspect ratios. Linearity of the governing equations permitted decomposition of solutions into pressure-driven and shear-driven components that were separately treated but may be superposed to represent any conditions of aiding or opposing forces. The pressure-driven solutions apply equally well to flows driven by capillary or gravity forces as well as applied pressures. Surface shear forces are sometimes important in parallel liquid–vapor flows arising in evaporative cooling devices, particularly when channel depths are relatively shallow.

The primary contribution of the present study is the derivation of analytical expressions that are very comprehensive in their range of application, yet remain relatively simple to apply and accurate within a few percent for most flow regimes of interest. Across the full range of flow conditions, relative errors are less than 15%.

These analytical approximations were constructed by blending of asymptotic solutions that apply in limiting regimes where the fluid depth at the channel centerline is either very small or very large compared to the channel width. In the deep limit, the flow resembles that between infinite parallel planes, but the solutions are qualitatively very different for pressure- and shear-driven flows. The mean speed of a pressure-driven flow approaches a constant value that is independent of the contact angle, whereas the mean speed of a shear-driven flow decreases linearly as the reciprocal of the relative fluid depth and has a persistent dependence on contact angle.

In the opposing limit of relatively shallow fluid layers the meniscus approaches the bottom of the channel, producing a pair of nearly disjoint corner flows. Because of symmetry about the channel centerplane, the apparent contact angle at the channel bottom is always 0°, whereas the contact angle at the side wall is arbitrary. These corner flows are modeled by blending of asymptotic solutions that apply in the limits of 0° and 90° contact angles. In the latter shallow-layer limit, the free surface is well approximated by a parabola and the mean speed increases with the wetting height on the side wall, either linearly or quadratically for the respective cases of shear- and pressure-driven flows.

When the meniscus actually contacts the channel floor, the flow must separate into a pair of corner flows having equal contact angles and, hence, equal wetted lengths on the bottom and side walls. These equilateral channel flows, previously studied in [8–10], are not the same as those discussed just above.

Although specific engineering applications have not been explored here, the present models are currently being used to investigate two important classes of problems, transient wetting behavior and steady evaporating flows. These applications are of increasing importance in a number of microscale applications including cooling of microelectronics, replication of MEMS devices by molding, and chip-based microchannel devices used for identification and synthesis of chemical and biological species.

Acknowledgements

This work was sponsored by the Engineering Sciences Research Foundation at Sandia National Laboratories. Sandia is a multi-program laboratory operated by Sandia Corporation, a Lock-heed Martin Company, for the United States Department of Energy under Contract DE-AC04-94AL85000.

Appendix A. Asymptotic solutions

In this appendix, we develop asymptotic solutions of the governing equations that apply in the limits of small and large aspect ratios, first for pressure-driven and then for shear-driven flows. The resulting velocity profiles are integrated over the flow domain to obtain the analytical expressions for mean velocity that are included in the main text.

A.1. Pressure-driven flow

The governing equations for the pressure-driven flow were given by Eqs. (14) and (15). In the limit as $\lambda \to 0$, the flow resembles that between closely spaced parallel plates. Thus, the derivatives of velocity with respect to depth are generally small compared to the cross-channel derivatives so that the velocity becomes a function of horizontal position alone.

$$u_p^*(x^*) = \frac{1}{2}\left(\tfrac{1}{4} - x^{*2}\right), \quad -1/2 \leqslant x^* \leqslant 1/2. \tag{A.1}$$

Although this expression does not apply to the boundary layers at the channel top and bottom, these regions become increasingly less important in the limit as $\lambda \to 0$. Substituting Eq. (A.1) into Eq. (19) and integrating over the domain yields the following asymptotic expression:

$$U^* = \frac{1}{12}. \tag{A.2}$$

Conversely, as the aspect ratio $\lambda \to \infty$ the layer becomes very shallow and the vertical shear stresses become large

compared to those in the cross-channel direction such that the velocity is a function of y alone, except in the relatively thin boundary layers on the side walls of the channel.

$$u_p^*(y^*) = \frac{1}{2\lambda^2} y^*(2 - y^*), \quad 0 \leqslant y^* \leqslant 1, \tag{A.3}$$

The integral of this expression over the flow domain is dependent upon the shape of the meniscus and the fluid depth at the center of the channel. Some special, but important, cases are presented below, followed by a more general result. For a contact angle of 90° the meniscus is flat and the integration yields

$$U^* = \frac{1}{3\lambda^2}. \tag{A.4}$$

This shallow-layer asymptote is shown in Fig. 5a along with the opposing deep-layer asymptote given in Eq. (A.2).

For contact angles smaller than 90° the flow geometry approaches a corner flow configuration like that shown in Fig. 2b as the layer becomes shallow. From Fig. 1 we see that when $h \to 0$, the free surface can be represented by

$$\left(\frac{x}{R}\right)^2 + \left(\frac{y}{R} - 1\right)^2 = 1, \tag{A.5}$$

where R is the radius of the free surface. As $\alpha \to 90°$, $R \to \infty$ and Eq. (A.5) can be approximated by

$$\left(\frac{x}{R}\right)^2 - 2\frac{y}{R} = 0, \tag{A.6}$$

or

$$y = \frac{x^2}{2R}, \tag{A.7}$$

where $R = W^2/8H$. Eq. (A.7) shows that when $h = 0$ and $\alpha \to 90°$ ($\Lambda \to \infty$), the free surface can be approximated by a parabola. This expression greatly simplifies the development of the right asymptote for the corner flows in Fig. 5b as shown next.

Let y and dx be the height and width of a fluid element at x, then the area, A, occupied by the fluid is

$$A = 2\int_0^{W/2} y\,dx = \frac{1}{3}WH. \tag{A.8}$$

As $\Lambda \to \infty$ ($\alpha \to 90°$) Eq. (A.4) suggests that each fluid element at x, of width dx and area $dA = y\,dx$, moves with an approximate average axial speed, U_x^*, given by

$$U_x^*(x) = \frac{1}{3\Lambda^2(x)}, \tag{A.9}$$

where $\Lambda(x) = W/y(x)$. The mean velocity over the entire fluid area is then

$$U^* = \frac{2}{A}\int_0^{W/2} U_x^*(x)\,dA = \frac{1}{7\Lambda^2}. \tag{A.10}$$

As noted earlier, Eqs. (A.4) and (A.10) are special cases of a more general expression that applies when the layer depth is small, but nonzero, and the meniscus is relatively flat. For that case, the liquid depth y in Eq. (A.7) is replaced by

$$y = h + \frac{x^2}{2R}, \tag{A.11}$$

where $R = W^2/8(H - h)$. The liquid area is then given by $A = (H + 2h)W/3$ and following the procedures used to obtain Eq. (A.10), the mean velocity becomes

$$U^* = \frac{\left(\frac{\Lambda}{\lambda}\right)^3 + \left(\frac{\Lambda}{\lambda}\right)^2 + \frac{3}{5}\left(\frac{\Lambda}{\lambda}\right) + \frac{1}{7}}{\left[1 + 3\left(\frac{\Lambda}{\lambda}\right)\right]\Lambda^2}, \tag{A.12}$$

where Λ and λ are defined by Eqs. (3) and (13), respectively. Clearly, in the limit as $\lambda \to \infty$, Eq. (A.12) reduces to Eq. (A.10) and as $\Lambda \to \infty$, Eq. (A.12) yields the expression obtained in Eq. (A.4).

A.2. Shear-driven flow

The governing equations for the shear-driven flow are given by Eqs. (16) and (17). When the fluid layer is relatively shallow and flat, Eq. (17) reduces to

$$\frac{\partial u_\tau^*}{\partial y^*} = \frac{1}{\lambda}. \tag{A.13}$$

The solution is given by

$$u_\tau^*(y^*) = \frac{1}{\lambda} y^*, \quad 0 \leqslant y^* \leqslant 1 \tag{A.14}$$

and the corresponding mean velocity is

$$U^* = \frac{1}{2\lambda}. \tag{A.15}$$

In the opposite limit of deep slender channels the influence of an aiding or opposing shear is localized near the free surface, but the flow field remains two-dimensional in that region. Therefore, to obtain the velocity profile, the complete two-dimensional equation given by Eq. (16) subject to boundary conditions given in Eqs. (8) and (A.13) must be solved analytically. Using the method of separation of variables, the velocity profile for a flat interface ($\alpha = 90°$) is given by

$$u_\tau^*(x^*, y^*) = \sum_{n=0}^{\infty} \frac{2[1 - (-1)^n]\sinh\left(\frac{n\pi}{\lambda} y^*\right)\sin(n\pi x^*)}{n^2\pi^2\cosh\left(\frac{n\pi}{\lambda}\right)}, \tag{A.16}$$

from which the mean velocity is obtained as

$$U^* = \lambda \sum_{n=0}^{\infty} \frac{2[1-(-1)^n]^2}{n^4\pi^4}\left[1-\cosh^{-1}\left(\frac{n\pi}{\lambda}\right)\right]. \qquad (A.17)$$

As $\lambda \to 0$, the hyperbolic cosine term in Eq. (A.17) vanishes and the remaining series of reciprocal powers sums to 1/12 (see [12]). Thus,

$$U^* = \frac{\lambda}{12}. \qquad (A.18)$$

When $\alpha \neq 90°$ the denominator of Eq. (A.18) is replaced by the function $c(\alpha)$ given in Eq. (30). Eqs. (A.15) and (A.18) are illustrated in Fig. 7a.

The corner flow asymptote for the shear-driven flow is obtained by following the procedure developed in Appendix A.1 to obtain the corner flow asymptote for the pressure-driven flow. As $\Lambda \to \infty$ ($\alpha \to 90°$), Eq. (A.15) suggests that each fluid element at x, of width dx and area $dA = y\,dx$, moves with an approximate average axial speed, U_x^*, given by

$$U_x^*(x) = \frac{1}{2\Lambda(x)}, \qquad (A.19)$$

where $\Lambda(x) = W/y(x)$. Integrating Eq. (A.19) over the entire fluid area gives

$$U^* = \frac{2}{A}\int_0^{W/2} U_x^*(x)\,dA = \frac{3}{10\Lambda}. \qquad (A.20)$$

As in the pressure-driven case, Eqs. (A.15) and (A.20) are special cases of the following more general expression that applies for large values of both λ and Λ.

$$U^* = \frac{\frac{3}{2}\left(\frac{\Lambda}{\lambda}\right)^2 + \left(\frac{\Lambda}{\lambda}\right) + \frac{3}{10}}{\left[1+3\left(\frac{\Lambda}{\lambda}\right)\right]\Lambda}. \qquad (A.21)$$

In the limit as $\lambda \to \infty$ Eq. (A.21) reduces to Eq. (A.20) and as $\Lambda \to \infty$, Eq. (A.21) yields the expression obtained in Eq. (A.15).

References

[1] G.E. Schneider, R. DeVos, Nondimensional analysis for the heat transport capability of axially-grooved heat pipes including liquid/vapor interaction, AIAA Paper No. 80-0214, 1980.

[2] G. DiCola, Soluzionne analitica, amezzo della transformata di fourier, di un problema di fusso in un canale rettangolare. Euratom C.C.R. Ispra (Italy), CETIS, 1968.

[3] J.S. Suh, R. Greif, C.P. Grigoropoulos, Friction in microchannel flows of a liquid and vapor in trapezoidal and sinusoidal grooves, Int. J. Heat Mass Transfer 44 (2001) 3103–3109.

[4] S.K. Thomas, R.C. Lykins, K.L. Yerkes, Fully developed laminar flow in trapezoidal grooves with shear stress at the liquid–vapor interface, Int. J. Heat Mass Transfer 44 (2001) 3397–3412.

[5] I. Catton, G.R. Stroes, A semi-analytical model to predict the capillary limit of heated inclined triangular capillary grooves, J. Heat Transfer 124 (2002) 162–168.

[6] J.M. Ha, G.P. Peterson, Analytical prediction of the axial dryout point for evaporating liquids in triangular microgrooves, ASME J. Heat Transfer 116 (1994) 498–503.

[7] H.B. Ma, G.P. Peterson, X.J. Lu, The influence of vapor–liquid interactions on the liquid pressure drop in triangular microgrooves, Int. J. Heat Mass Transfer 27 (1994) 2211–2219.

[8] P.S. Ayyaswamy, I. Catton, D.K. Edwards, Capillary flow in triangular grooves, ASME J. Appl. Mech. 41 (2) (1974) 332–336.

[9] T.C. Ransohoff, G.J. Radke, Laminar-flow of a wetting liquid along the corners of a predominantly gas-occupied noncircular pore, J. Colloid Interface Sci. 121 (2) (1988) 392–401.

[10] L.A. Romero, F.G. Yost, Flow in an open capillary channel, J. Fluid Mech. 322 (1996) 109–129.

[11] E.W. Becker, W. Ehrfeld, P. Hagmann, A. Maner, D. Munchmeyer, Fabrication of microstructures with high aspect ratios and great structural heights by synchrotron radiation lithography, galvanoforming, and plastic molding (liga process), Microelectron. Eng. 4 (1986) 35–56.

[12] M. Abramowitz, I.A. Stegun, Handbook of Mathematical Functions, Bernoulli and Euler Polynomials, second ed., National Bureau of Standards, Washington, DC, 1964, p. 108.